# Harnessing plasma absorption in silicon MOS modulators

**Weiwei Zhang**
University of Southampton https://orcid.org/0000-0002-1086-5775
**Martin Ebert**
University of Southampton
**Ke Li**
University of Southampton https://orcid.org/0000-0002-2954-1383
**Bigeng Chen**
University of Southampton
**Xingzhao Yan**
University of Southampton
**Han Du**
University of Southampton
**Mehdi Banakar**
University of Southampton
**Dehn Tran**
University of Southampton
**Callum Littlejohns**
University of Southampton
**Adam Scofield**
Rockley Photonics
**Guomin Yu**
Rockley Photonics
**Roshanak Shafiiha**
Rockley Photonics
**Aaron Zilkie**
Rockley Photonics
**Graham Reed**
University of Southampton
**David Thomson** ( d.thomson@soton.ac.uk )
University of Southampton https://orcid.org/0000-0002-1838-2663

**Article**

**Keywords:**

**Posted Date:** May 12th, 2022

**DOI:** https://doi.org/10.21203/rs.3.rs-1618900/v1



**Version of Record:** A version of this preprint was published at Nature Photonics on February 20th, 2023. See the published version at https://doi.org/10.1038/s41566-023-01159-3.

# Abstract

High bandwidth, low power and compact silicon electro-optical modulators are essential for future energy efficient and densely integrated optical data communication circuits. The all-silicon plasma dispersion effect ring resonator modulator is an attractive prospect. However its performance is currently limited by the trade-off between modulation depth and switching speed dictated by its quality factor. Here we introduce a mechanism to leap beyond this limitation by harnessing the significant plasma absorption induced in a silicon MOS waveguide to enhance the extinction ratio of a low quality factor, high-speed ring modulator. Fabricated devices have demonstrated 20dB of electro-absorption modulation at the resonance with a 3.5V bias change and a total modulation depth of 27dB with the concurrent carrier refraction induced wavelength shift. Modulation enhancement has been observed from kHz to GHz operation with data modulation up to 100Gbit/s on-off keying demonstrated, paving the evolution of optical interconnects to 100Gbaud and beyond per wavelength.


# Introduction

Integrated electro-optic modulators offer huge potential to meet the rapidly growing bandwidth requirements of communications and computations. Devices based upon silicon, allow high volume, low cost CMOS fabrication and co-integration with the required drive and control electronics and are therefore promising candidates for mass producible Tb/s-scale inter-rack and intra-rack interconnects [1–4]. With the relentless demand for more and more bandwidth, the requirements of the optical modulator become increasingly stringent and simultaneously satisfying all of the different performance metrics including high speed, low power consumption, high extinction ratio, compactness and low optical loss is a major challenge. For example, the commonly deployed carrier depletion based Mach–Zehnder interferometer (MZI) modulator can operate at high speeds but is relatively inefficient resulting in devices that require a large driving power and/or length to achieve a sufficient extinction ratio. This has motivated a wide range of research activities towards the incorporation of materials with stronger electro-optic effects onto silicon photonic waveguides including $LiNbO_3$(LN) [5,6], BaTiO3(BTO) [7], lead zirconate titanate (PZT) [8], EO polymers [9,10], GeSi and Ge/SiGe quantum wells (QW) [11–13] as well as III-V material compounds [14]. Whilst these approaches have demonstrated some promising performances, the introduction of these different materials inevitably complicates the fabrication process and in many cases conflicts with CMOS compatibility.

Another alternative to the MZI modulator is a resonant approach such as the ring resonator modulator. Such devices have real prospects in meeting future needs in terms of compactness, loss and drive power. Recently, demonstrations have shown that on-chip control of the device operation can efficiently negate issues with thermal stability and fabrication tolerance sensitivity in aligning the resonance with the required operating wavelength [15,16]. A major challenge with ring modulators is surpassing performance limitations that arise from selection of an appropriate quality factor (Q-factor) dictating the trade-off between the speed of modulation and the achievable extinction ratio (ER). A high *Q*-factor gives spectrally

narrower resonance requiring a smaller wavelength shift for a large ER, however, the longer photon cavity lifetime that results limits switching speeds.

Here we introduce a technique to enhance the ER in ring resonator modulators through the combination of electro-refraction and electro-absorption modulation within a polysilicon/$SiO_2$/Si MOS waveguide. Electro-absorption can enhance the ER produced by the electro-refractive shift of the resonant wavelength allowing for use of a lower *Q*-factor ring that can then produce both high speed modulation together with a large modulation depth, hence jumping beyond previous limitations. The degree of carrier based electro-absorption within a device providing a given phase shift has a superlinear relationship with carrier density[17]. The strong electro-absorption demonstrated is therefore unique to MOS waveguide modulators where the accumulated free carriers are dense and highly localized. The resultant change in absorption is therefore significantly weaker in carrier depletion modulators where the change of carrier density is typically at least an order of magnitude lower. The application of an electrical bias to the MOS waveguide incorporated into a ring resonator can substantially detune the coupling conditions between over coupling, critical coupling and weak coupling resulting in large changes in optical transmission at the resonance, whilst the resonance position is also shifted in wavelength. This absorption also benefits the speed of carrier accumulation which is also heavily influenced by the device capacitance since the absorption effectively reuses the same carriers that cause the electro-refractive resonance shift, allowing for a reduced device capacitance for the same degree of modulation.

Fabricated devices have demonstrated 20dB modulation at the resonance with a 3.5V reverse bias (or 4V forward bias) through the carrier absorption effect alone making the silicon MOS ring resonator modulation analogous to previously demonstrated graphene-MOS ring resonator EAMs[18], where 15dB absorption was measured with 10V gate voltage change. When operated at an insertion loss point of 3.3dB the co-operation of the carrier refraction and absorption effects, allows an intensity variation of 27dB with a voltage change ($\Delta V_g$) of 3.5V or 4V in reverse and forward bias respectively. At high speed, the MOS ring modulator can work in the accumulation/inversion regimes with an EO bandwidth of 50GHz or above with operation demonstrated at a data rate ≥ 100Gb/s non-return-to-zero (NRZ).

# Device Design

The device is based in 220nm high silicon-on-insulator waveguides. The inside rail of the ring is formed of polysilicon doped with boron (Fig. 1a). The outer rail is formed of single crystal silicon side and doped with phosphorus. The cross-section of the MOS-junction has been characterized using a transmission electron microscope (TEM) (Fig. 1c), indicating polysilicon grain sizes in the range of a few 10's nm to several 100 nm and a gate oxide thickness of ~ 5.5nm (See supplementary section-II). Bent bus waveguides were used in the coupling region (Fig. 1b) to enhance coupling with the resonator. The modulator of cross-section as depicted in Fig. 1d has been incorporated into a ring with 15μm radius (R). The optical losses measured at 1550nm for straight 450nm wide MOS rib waveguides before and after doping are ~ 8.6dB/cm and ~ 38dB/cm respectively. For comparison undoped rib waveguides of the same width have losses of 1.8dB/cm for silicon and 25dB/cm for polysilicon. The high loss of the

polysilicon is not detrimental to the ring modulator, as low *Q*-factor resonators are required for high bandwidth modulation.

## Dc Response

Normalised optical spectra with different gate voltages ($V_g$) applied from − 5V to 6V are shown in Fig. 2.a-d. A set of devices with variations in the gap between the resonator and bus waveguide from 200nm to 400nm were fabricated providing a range of coupling conditions from over coupled to under coupled. For devices initially over coupled at $V_g$=0V, the bus ring gap is typically 210nm to 250nm (see supplementary section-I). The analysis here forth was performed on a device with 230nm gap and loaded *Q*-factor in the range of 3,450 to 4,600. As discussed above, contrary to typical depletion-type ring modulators, the transmission spectrum of our MOS ring resonators shows both strong resonance depth modulation and resonance shift (Fig. 2.c and 2.d). The application of a forward (Fig. 2.a) or reverse bias $V_g$ (Fig. 2.b), gives a resonance blue shift ($\Delta\lambda/\Delta V_g$) of around 40pm/V, due to a carrier concentration increase in both accumulation and inversion modes. The modulation phase change efficiency is estimated to be no more than 1.3V•cm for both inversion and accumulation modes when $|V_g| \leq 2V$ and approximately 0.7V•cm for $|V_g| > 2V$. The increased carrier concentration also induces a large optical absorption that substantially detunes the coupling condition of the ring. With $\Delta V_g$ varied over 4V, the coupling condition can change between over, critical and under coupling (See supplementary section-I). The resonance depth increases from ~ 10dB to ~ 30dB with a $\Delta V_g$ of 3.5V in reverse bias or 4V in forward bias respectively (Fig. 2.c and 2.d). By fitting the ring transmission Eq. 1[9], the extracted propagation losses (α) for the bent MOSCAP waveguides increases from 45dB/cm to 95dB/cm when $V_g$ changes from to 0V to 5V or to -6V (Fig. 2.e), agreeing well with the simulated Δα of 50dB/cm (See supplementary section-I). The single circulation amplitude attenuation factor of the ring (*a*), which is defined as $a^2 = \exp(-\alpha 2\pi R)$ is tunable in the range of 0.95 to 0.9 (Fig. 2.f). The self-coupling coefficient *t* between the bus waveguide and ring is constant at ~ 0.9. Hence, the applied gate voltage $V_g$ can tune the coupling condition from over coupling to critical coupling ($a = t$) through controlling the internal loss of the MOS ring resonator.

Analysis of the MOS junction with double direction sweeping of $V_g$ has been performed to confirm resonance shifts are not induced by other MOS interface charges, mobile charges or other kinds of imperfection, etc., as observed in other integrated silicon devices [7, 20–22]. No optical hysteresis has been observed, meaning that the capacitance of MOS junction is stable and minimal parasitic defects exist in the device (see supplementary section-I). The large carrier induced absorption is repeatable across numerous devices in different dies and wafers. The lowest $\Delta V_g$ required to achieve 20dB transmission change at the resonance wavelength was found to be 3V, with 28dB ER modulation at the carrier wavelength with an IL of 2.3dB (See supplementary section-I).

The loaded resistance and capacitance at $V_g$ = 0V is 37Ω and 38fF, respectively, leading to an electrical intrinsic RC bandwidth ($BW_E$) of 113GHz (See supplementary section-III) (source impedance excluded).

Simulations predicts the total capacitance for the loaded 83μm long MOSCAP segment increases from 47fF to, 89fF, 107fF and 112fF with $V_g$ increases from 0V to 1V, 2V and 4V, respectively. An increased forward bias voltage will therefore reduce the intrinsic $BW_E$ down to 38GHz at $V_g$=4V. Nevertheless, the bandwidth limitation can be overcome by reducing the MOSCAP segment length that is demonstrated hereafter.

# Plasma Absorption Assisted Intensity Modulation

The additional resonance depth modulation results in a substantial enhancement of the ER (ER+) on one side of the resonance whilst suppression (ER-) occurs on the other side. This can be observed in Fig. 2.c and 2.d where the transmission differences between different gate voltages on the left side of the resonance are much larger than on the right. Figure 2h further indicates this by directly plotting the change in transmission with voltage for our experimental case together with two artificial cases which have the same degree of spectral resonance shift but no resonance depth variation (i.e. no absorption modulation). For the two artificial cases *a* is kept constant at 0.9 and 0.95 which represent the two extremes of our experimental case with the largest and smallest resonance depth respectively. Starting from same IL point (1.8dB), for our experimental case with variable *a*, the gate voltage induced transmission change is substantially larger compared to both cases with fixed *a*. Figure 2.h also shows that the change in transmission for the experimental case when operating at the “ER-“ point is much lower than for the “ER+“ case as well as the two artificial cases. The cases with fixed *a* are closer to what is usually observed in carrier depletion based silicon ring modulators. As a result, demonstrated carrier depletion based ring modulators which achieve a larger spectral shift for a given voltage compared to our device show an inferior DC modulated ER[23].

ER enhancement has also been investigated at high speed (250kHz to 5GHz) by applying sinusoidal signals of 3V amplitude to the device (Fig. 3). The MOS junction is biased at Vg = -4V for the inversion mode and Vg = + 4V for accumulation mode. The wavelength is chosen at right side of the resonance with IL of 6dB for the “ER-” operating point and the left side with IL of 6dB for the “ER+” point. Figure 3.b plots the measured ER against frequency for the “ER-” and “ER+” operating points for both inversion and accumulation operation. A difference in the ER between the two operating points demonstrates the absorption based enhancement and suppression effects. Without enhancement or suppression the extinction ratio would be the same at the “ER-” and “ER+” operating points on either side of the resonance and the ER value would be between those achieved with enhancement and suppression. For the inversion mode, the MOS junction model [24] tells us that the carrier accumulation is much slower and therefore the density of carriers reduces with increasing frequency and with this the contribution of carrier absorption and resultant ER enhancement becomes much less significant. This is evident in Fig. 3.b where a difference in ER for the two operating points can only be observed for frequencies below 10MHz. For the accumulation mode a difference in the ER for the “ER+” and “ER-” plots extends over the entire measured frequency range. Figure 3.c & d directly demonstrates the enhancement and suppression in ER that results when the modulator is operating at a data rate of 10Gbit/s. Figure 3.c is the optical eye diagram

that is measured at the “ER-” point where an ER of 3.2dB is recorded and Fig. 3.d is at the “ER+” point with an ER of 5.8dB. The carrier absorption induced enhancement in ER can clearly be seen and compared for both operating modes, proving that accumulated dense carriers can respond at high frequencies in accumulation mode allowing plasma absorption enhancement in a high speed silicon MOS modulator.

## High Speed Operation

The high speed performance depends on the electrical bandwidth, the photonic cavity lifetime of the ring as well as any peaking effects that can result from detuning the operating wavelength away from the ring’s resonance. Besides enhancing the ER, the large carrier absorption modulation can also help to lower the Q of the device which in turn can increase the photon lifetime limited modulation bandwidth $f_{ph}$ (~3dB bandwidth of spectrum). For instance, $f_{ph}$ is 46GHz for $V_g$ = 0V, and 60GHz for $V_g$ = 6V. When the wavelength is detuned from the resonance, optical peaking enhancement in high-speed ring modulators can also extend the bandwidth of the actual response beyond the simple photon lifetime and RC model predictions [25].

The device has been characterized at high speed first by measuring the electro-optic S21 using a lightwave component analyzer (LCA) (Fig. 4.a). In accumulation mode the EO bandwidth is highly dependent on the device capacitance which varies significantly with gate voltage. The measured bandwidth of the device with 83μm segment in accumulation mode is ≥50GHz with $V_g$ ≤1V and an IL of 3dB (Fig 4.c). With $V_g$ set ≥ 2V, the EO bandwidth drops to less than 10GHz. Beyond 2V the peaking effect is no longer strong enough to compensate the roll-off due to the large capacitance. The peaking effect is more prominent in the EO bandwidth curves of the shorter (25μm), lower capacitance MOSCAP segment where an EO bandwidth ~50GHz was measured in accumulation mode with $V_g$ up to 2V (Fig 4.c). A 25μm length corresponds approximately to the circumference of a ring with 4μm radius or, for a segmented PAM-4 modulation approach [23], the length of one of two segments implemented in a ring with 10μm radius. In accumulation mode, (optical eye diagrams at 64Gbit/s were measured from the 83μm segment with a 3dB ER with $V_g$=1V and RF $V_{pp}$=2V using the setup shown in Fig 4.b.

At higher speed (100Gbaud), both small and large signal testing were carried out to verify the high-speed transmission rate limits. The input RF to optical link signal integrity was analyzed as summarized in Table.1. The initial seed signal at 100Gbit/s from an SHF MUX output has an amplitude ~500mV and signal to noise ratio (SNR) ~15. With the signal passed through a 50cm long RF cable and fed into a 60GHz amplifier to increase the amplitude to ~2.5V the SNR had dropped to 3.8. The signal was then passed through a 65GHz bias tee and 50 Ω terminated probe to drive the MOS ring modulator. As shown in Table.1, the quality of the signal at the output of the probe is further degraded. The measured optical eye diagram quality is dependent on the amount of wavelength detuning from the resonance (or IL) [25]

and bias voltage. The received optical eye diagrams are shown in Table 1 when the operating point is set to an optical power loss of 6dB and with a driving voltage of $V_{pp}$ 1.6V. The optical eye is further open after feed-forward error correction to compensate the bandwidth limitations and nonlinearity dynamics due to large signal driving. A 3-tap feed forward equalizer (FFE) enabled in the detection of the DCA allows open eye diagrams with a bit error rate (BER) measured in jitter mode at a level of 1e-4 and 4e-6 for received optical powers of 2mW and 8mW, respectively.

The design of current fabricated devices is not optimized. To further improve the ring performance, the radius can be reduced to 5μm or less which allows for a smaller MOSCAP segment with lower capacitance as discussed above. In this way, higher bias voltages can be used with a reasonable capacitance level retained, enabling stronger absorption enhancement at high speed. The electrical structure including the polysilicon section of the device can support high speed operation with lower capacitance. Experimentally, this is demonstrated by driving the modulator with a reverse bias of $V_g$=-5V, where the loaded capacitance is close to that at Vg=0V. In this case fully open optical eye diagrams can be measured at 100Gb/s with SNR range of 2 to 3 an optical IL < 6dB. The optical modulation ER can reach up to 3.6dB when one level insertion loss is 9dB with RF swing 1.6V and the whole setup and device allows a highest NRZ operating speed of 112Gb/s (see supplementary section-IV). Access resistance can be reduced if needed with a higher doping dose with the additional loss can compensated by using an optimized low loss polysilicon recipe [26,27]. Improvements in electrode design, optimized for high speed operation and the use of a dedicated drive amplifier can enable improved high speed performance [28,29]. The oxide thickness of the MOSCAP can also be adjusted to be thinner for integration with small voltage drivers. Thermal heaters with feedback control circuits can be introduced for more stable modulation, with a cleaner eye diagram [16].

# Conclusion

A mechanism to enhance the performance of all-silicon free carrier based ring modulators through the combination of carrier absorption and refraction effects has been introduced. The enhancement is largely unique to free carrier accumulation based devices due to the very dense accumulation of free carriers. Measurements have shown substantial detuning of the coupling condition allowing a 20dB change in output intensity with a gate voltage change of just 3.5V. The co-operation of carrier absorption and refraction circumvents design limitations ($V_\pi L$) of silicon modulators and makes the MOS silicon ring modulator highly competitive with other types of modulator towards small footprint, high bandwidth and low power consumption all whilst being producible using a reliable CMOS compatible fabrication process, avoiding complications through hybrid material integration. In summary the absorption enhanced silicon MOS ring modulator has excellent prospects for optimization towards low drive voltage, large ER and high bandwidth modulation paving the way for range of densely integrated applications

from low power switching in programmable photonics to high-speed data communication in optical interconnects.

# Declarations

Acknowledgements.

This work was supported by funding from Rockley Photonics and the EPSRC through the prosperity partnership (EP/R003076/1), EPSRC Platform Grant (EP/N013247/1); EPSRC Strategic Equipment Grant (EP/T019697/1) and European Commission H2020 PICTURE Project (780930). D. J. Thomson acknowledges funding from the Royal Society for his University Research Fellowship (UF150325).

Author contributions.

W. Zhang contributed to the idea, simulation, fabrication, device testing and manuscript preparation. K. Li contributed to device testing. M. Ebert, B. Chen, X. Yan, H. Du, M. Banakar, D. Tran, C. Littlejohns contributed to device fabrication. A. Scofield, G. Yu, R. Shafiiha, A. Zilkie, G. Reed contributed to the discussion, and Reed manages the Silicon Photonics Group at Southampton. D. J Thomson provided high-level project supervision, and manuscript revision.

Competing financial interests

The authors declare no competing financial interests.

# Methods

***Fabrication.*** The passive MOS junction fabrication process started with thermal growth of 30 nm of silicon dioxide on the thin silicon overlayer followed by DUV-248 scanner lithography and etching to form trenches for polysilicon infilling. MOS junction was formed by another dry thermal oxide growth after trench etching, after which polysilicon was deposited by low pressure chemical vapor deposition (LPCVD) and annealed at 1000°C for 10 hours in a nitrogen atmosphere. A chemical mechanical polishing process was then used to planarize the wafer down to the 30 nm thermal oxide stopping layer on the Si overlayer. The MOS ring, bus waveguides, grating coupler structures were then patterned by DUV-248 scanner lithography and inductively coupled plasma (ICP) etching. The silicon and polysilicon were then doped with light and heavy p and n regions. A 1um thick silicon dioxide layer was then deposited by PECVD followed by a further lithography and etching step to open vias down to the heavily doped regions. Metal was then deposited and etched through a resist mask formed again by DUV-248 lithography to form the device electrodes.

***High-speed test.*** The setup used for measuring the optical eye diagrams is shown in Fig.3. Two electrical signals (PRBS $2^7$-1) generated by a SHF bit pattern generator (BPG) (12104A) were sent to a SHF 603B MUX, which provided a seed signal at data rates up to 112Gb/s. The clock generator used was an Agilent

E8257D. The seed signal was subsequently passed through a half meter 67GHz cable, 60 GHz amplifier (SHF S804), 65 GHz bias tee, and 50 Ω terminated 67 GHz GGB GSG probe. The light after the output grating coupler was amplifier by an erbium doped fiber amplifier (EDFA). After the EDFA, the optical noise was suppressed using a bandpass (3nm) filter before being fed into a Keysight Digital Communication Analyzer (Keysight Infiniium DCA-X 86100D with Agilent 86116C-040 plugin module). The electrical signal embedding was carried out by the software functions of DCA, as well. The electrical response (S11) was measured by an Agilent E8361A 67GHz network analyser after calibration. The electro-optical response (S21) was measured by using a Keysight N4373E Lightwave Component Analyzer with a 67GHz frequency range. The optical eye diagrams for the MOS inversion mode were measured under a DC reverse bias of 5V. The input electrical eye diagrams at data rates of 64Gb/s, 100 Gb/s and 112 Gb/s are shown in supplementary material section-IV.

Data availability.

The data that support the plots within this paper and other findings of this study are available from the corresponding authors upon reasonable request. Alternatively, all data supporting this study are available upon request from the University of Southampton repository at https://doi.org/10.5258/SOTON/D1909

# References


1. Reed, G. T., Mashanovich, G., Gardes, F. Y. & Thomson, D. J. Silicon optical modulators. Nature Photonics vol. 4 518–526 (2010).
2. Thomson, D. *et al.* Roadmap on silicon photonics. J. Opt. **18**, 073003 (2016).
3. Reed, G. T. *et al.* Recent breakthroughs in carrier depletion based silicon optical modulators. Nanophotonics **3**, 229–245 (2014).
4. Rahim, A. *et al.* Taking silicon photonics modulators to a higher performance level: state-of-the-art and a review of new technologies. Adv. Photonics **3**, 1–23 (2021).
5. Wang, C. *et al.* Integrated lithium niobate electro-optic modulators operating at CMOS-compatible voltages. Nature **562**, 101–104 (2018).
6. He, M. *et al.* High-performance hybrid silicon and lithium niobate Mach–Zehnder modulators for 100 Gbit s -1 and beyond. Nat. Photonics **13**, 359–364 (2019).
7. Abel, S. *et al.* Large Pockels effect in micro- and nanostructured barium titanate integrated on silicon. Nat. Mater. **18**, 42–47 (2019).
8. Alexander, K. *et al.* Nanophotonic Pockels modulators on a silicon nitride platform. Nat. Commun. **9**, 4–9 (2018).
9. Kieninger, C. *et al.* Ultra-high electro-optic activity demonstrated in a silicon-organic hybrid modulator. Optica **5**, 739 (2018).
10. Lu, G. W. *et al.* High-temperature-resistant silicon-polymer hybrid modulator operating at up to 200 Gbit s – 1 for energy-efficient datacentres and harsh-environment applications. Nat. Commun. **11**, 1–

9 (2020).

11. Srinivasan, S. A. *et al.* 60Gb / s waveguide-coupled O-band GeSi quantum-confined Stark effect electro-absorption modulator. Opt. Fiber Commun. Conf. *2021* 3 (2021).
12. Mastronardi, L. *et al.* High-speed Si/GeSi hetero-structure Electro Absorption Modulator. Opt. Express **26**, 6663 (2018).
13. Srinivasan, S. A. *et al.* 56 Gb/s Germanium Waveguide Electro-Absorption Modulator. J. Light. Technol. **34**, 419–424 (2016).
14. Han, J. H. *et al.* Efficient low-loss InGaAsP/Si hybrid MOS optical modulator. Nat. Photonics **11**, 486–490 (2017).
15. Jayatilleka, H. *et al.* Post-Fabrication Trimming of Silicon Photonic Ring Resonators at Wafer-Scale. J. Light. Technol. **39**, 5083–5088 (2021).
16. Li, H. *et al.* A 3-D-Integrated Silicon Photonic Microring-Based 112-Gb/s PAM-4 Transmitter with Nonlinear Equalization and Thermal Control. IEEE J. Solid-State Circuits **56**, 19–29 (2021).
17. Soref, R. & Bennett, B. Electrooptical effects in silicon. IEEE J. Quantum Electron. **23**, 123–129 (1987).
18. Phare, C. T., Daniel Lee, Y.-H., Cardenas, J. & Lipson, M. Graphene electro-optic modulator with 30† GHz bandwidth. Nat. Photonics **9**, 511–514 (2015).
19. Nitkowski, A., Chen, L. & Lipson, M. Cavity-enhanced on-chip absorption spectroscopy using microring resonators. Opt. Express **16**, 11930 (2008).
20. Abel, S. *et al.* A hybrid barium titanate-silicon photonics platform for ultraefficient electro-optic tuning. J. Light. Technol. **34**, 1688–1693 (2016).
21. Sharif Azadeh, S., Merget, F., Nezhad, M. P. & Witzens, J. On the measurement of the Pockels effect in strained silicon. Opt. Lett. **40**, 1877 (2015).
22. Sharma, R., Puckett, M. W., Lin, H. H., Vallini, F. & Fainman, Y. Characterizing the effects of free carriers in fully etched, dielectric-clad silicon waveguides. Appl. Phys. Lett. **106**, (2015).
23. Sun, J. *et al.* A 128 Gb/s PAM4 Silicon Microring Modulator With Integrated Thermo-Optic Resonance Tuning. J. Light. Technol. **37**, 110–115 (2019).
24. Hu, C. *Modern semiconductor devices for integrated circuits*. (Prentice Hall Upper Saddle River, NJ, 2010).
25. Müller, J. *et al.* Optical Peaking Enhancement in High-Speed Ring Modulators. Sci. Rep. **4**, (2014).
26. Zhang, W. *et al.* Integration of low loss vertical slot waveguides on SOI photonic platforms for high efficiency carrier accumulation modulators. Opt. Express **28**, 23143 (2020).
27. Zhu, S., Lo, G. Q., Ye, J. D. & Kwong, D. L. Influence of RTA and LTA on the optical propagation loss in polycrystalline silicon wire waveguides. IEEE Photonics Technol. Lett. **22**, 480–482 (2010).
28. Li, K. *et al.* Electronic–photonic convergence for silicon photonics transmitters beyond 100 Gbps on–off keying. Optica **7**, 1514 (2020).

29. A. Hashemi Talkhooncheh, W. Zhang, M. Wang, D. J. Thomson, M. Ebert, L. Ke, G. T. R. & Emami, A. A 2.4pJ/b 100Gb/s 3D-Integrated PAM-4 Optical Transmitter with Segmented SiP MOSCAP Modulators and a 2-Channel 28nm CMOS Driver. in *ISSCC 2022* (2022).

# Tables

Table 1 is in the supplementary files section.

# Figures

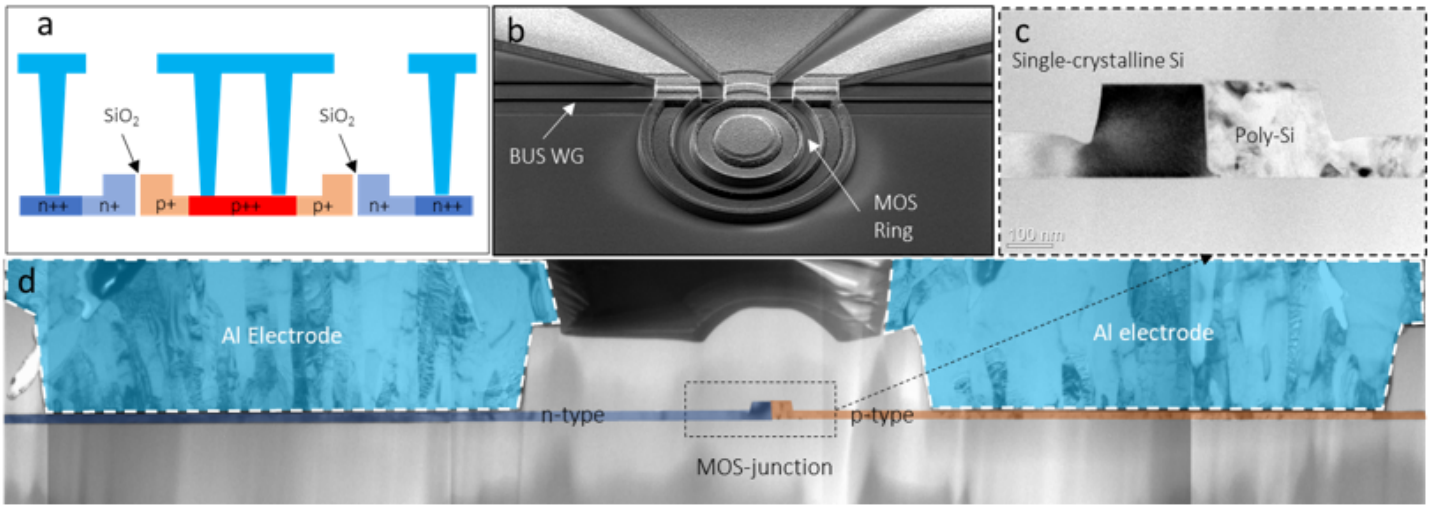


**Figure 1**

**Integrated silicon MOS modulator. a**, Cross-section schematic of the polysilicon/Si MOS capacitor ring resonator modulator design. **b**, Scanning electron microscope image of the fabricated MOS ring resonator modulator. The bus waveguide and ring positions are labelled. **c**, Transmission electron microscope image of the polysilicon/$SiO_2$/Silicon MOS rib waveguide. **d**, Transmission electron microscope image of the cross-section of the whole MOS junction including electrodes contacting the highly doped p and n regions.

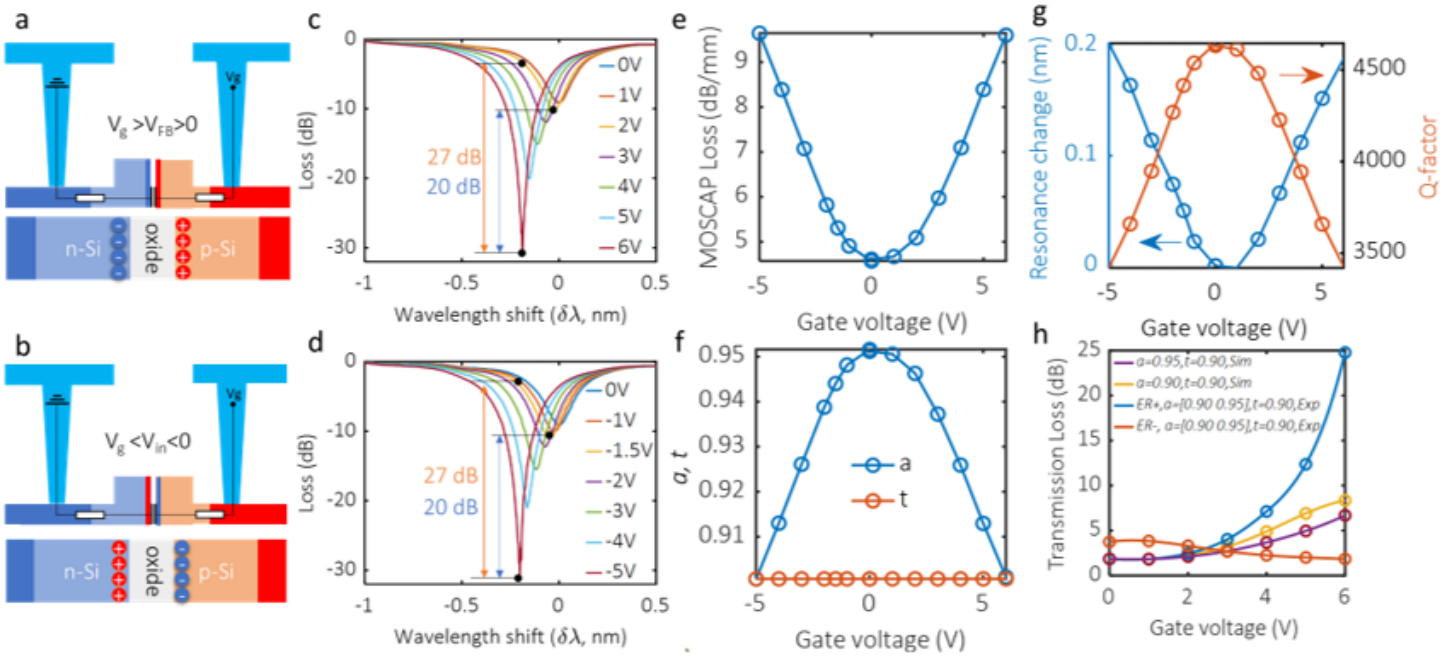


## Figure 2

**Static EO response of the MOS ring modulator.** (a) Schematic drawing of modulator working at $V_g > V_{FB}$ (MOS flat band voltage) indicating where carrier accumulation happens in the MOS accumulation mode. (c) Measured spectral response for $V_g \geq 0$ V. (b) Schematic drawing of MOS working at $V_g \leq V_{in}$ (MOS inversion voltage) indicating where carrier accumulations happen in the MOS inversion mode. (d) Measured spectral response for Vg ≤ 0 V. (e-f) show the gate voltages VS MOSCAP ring propagation loss in (e), single circulation amplitude attenuation factor *a* and the self-coupling coefficient *t* in (f), *Q*-factors and resonance wavelength changes in (g). Transmission loss in different situations are compared in (h). For carrier wavelength with “ER+” effect, one level IL starts from 1.8 dB and then significantly increases to 25 dB. While for the “ER-” effect, the IL changes between 1.8 dB and 3.8 dB.

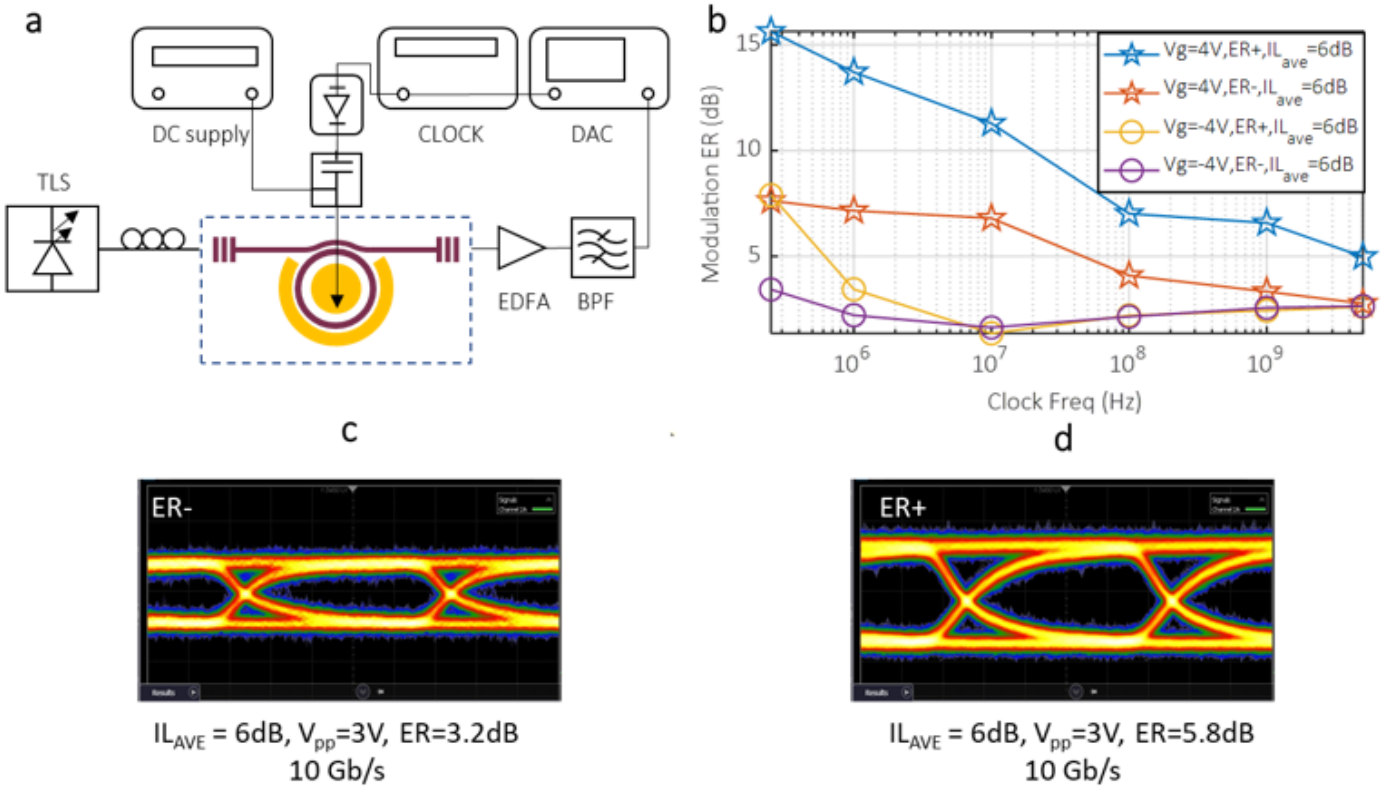


## Figure 3

**Frequency response of absorption enhancement.** (a) Setup used to measure the modulation ER of the electro-optic modulation in different operation modes. EDFA, erbium-doped fiber amplifier. BPF, band pass filter. DCA, Digital Communication Analyzer (DCA 86100D). TLS, tunable laser source. CLOCK, clock signal generator. (b) Comparison of the high speed response of the two effects “ER+”, “ER-” in accumulation mode (Vg=4V) and inversion mode (Vg=-4V). Measured optical eye diagrams in accumulation mode at data rate of 10 Gb/s with “ER-” effect (c) and “ER+” effect (d), with gate voltage at 4V and RF Vpp=3V and optical IL 6dB.

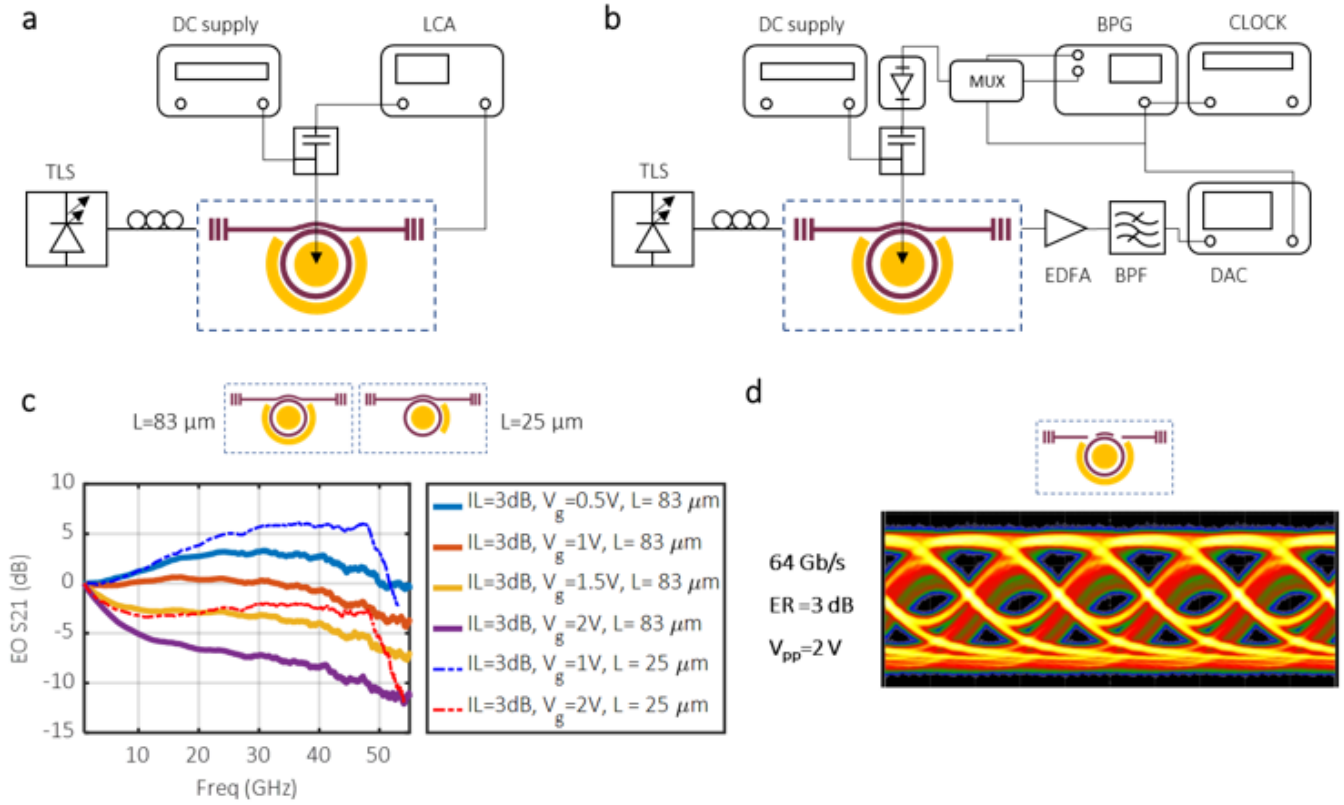


**Figure 4**

**EO bandwidths of inversion and accumulation modes.** (a) Setup used to measure the EO bandwidth of the ring resonator. LCA, lightwave component analyzer. (b), Setup used to test data transmission of the electro-optic modulation. EDFA, erbium-doped fiber amplifier. BPF, band pass filter. DCA, Digital Communication Analyzer (DCA 86100D). BPG, bit pattern generator (SHF 12104A). MUX (SHF 603B). TLS, tuneable laser source. (c), Measured and normalized EO bandwidth of the MOS ring resonator modulator with $V_g$ at 0.5V-2V with different lengths of active segments 25 µm and 83 µm. (d), Measured optical eye diagram with average at data rate of 64 Gb/s for MOSCAP ring modulator with active length 83 µm.

# Supplementary Files

This is a list of supplementary files associated with this preprint. Click to download.

- Table1.docx
- Finalsupplementarydata0413.docx